Article

Comparative Study of Dispersion Curves for LAMB Waves Using Analytical Solutions and Semi-Analytical Methods

Carlos A. Galán-Pinilla [1,*], Jabid E-Quiroga [2], Dario Y. Peña-Ballesteros [3], César A. Acosta-Minoli [4] and Octavio Andrés González-Estrada [2]

[1] GIMAT, School of Metallurgical Engineering, Universidad Industrial de Santander, Bucaramanga 680002, Colombia
[2] GIEMA, School of Mechanical Engineering, Universidad Industrial de Santander, Bucaramanga 680002, Colombia
[3] GIC, School of Metallurgical Engineering, Universidad Industrial de Santander, Bucaramanga 680002, Colombia
[4] GEDES, Universidad del Quindío, Armenia 630004, Colombia
[*] Correspondence: carlos.galan@correo.uis.edu.co; Tel.: +57-313-201-1885

Abstract: Lamb wave dispersion curves are useful for optimizing the inspection scanning distance that can be covered with good sensitivity in many current applications. However, one of the main problems concerning this calculation lies in selecting a numerical method that is computationally accurate and efficient. In this paper, Lamb waves dispersion curves are generated by the Scaled Boundary Finite Element Method, and by the Rayleigh–Lamb equation. For the semi-analytical case, waveguide cross-section discretization was performed using isoparametric elements and high-order spectral elements. The semi-analytical formulations lead to an eigenvalue problem that can be solved efficiently by calculating the couples of wavenumbers and frequencies that guarantee the wave mode propagation, the basis for generating the dispersion curves. These are compared with those obtained from the analytical solution for the symmetric and antisymmetric modes; in both cases, homogeneous plates of constant thickness are considered. The numerical results show good agreement when using a low number of isoparametric elements, or a single spectral element with shape functions of the order of six for computing the dispersion curves and wave structure. The calculation is given with low computational effort, and the relative variation with respect to the analytical reference values is less than 2%.

Keywords: dispersion curves; scaled boundary finite element method (SBFEM); guided waves ultrasonic testing (GWUT); high-order spectral elements; computational effort

1. Introduction

Lamb waves are waves whose material boundary is constrained and generated by the specimen's elastic micro-deformations, which propagate in parallel plate-like structures at ultrasonic frequencies with wavelengths λ, generally greater than the plate-thickness [1]. These waves have been of great interest in recent years in the field of nondestructive testing (NDT) [2–4], surface corrosion damage in plates [5,6], Structural Health Monitoring (SHM) [7], Lamb wave interaction with defects [8], and materials characterization [9]. It is possible to inspect over long distances, covering the entire cross-section of the plate from a single probe position, including isolated or embedded areas, which are of interest in many engineering applications for corrosion monitoring [10], monitoring stress levels [11], or aerospace composites [12]. Multiple symmetric *Sn* or antisymmetric *An* (*n* = 0, 1, 2, . . .) modes are generated for specific plate thicknesses, frequency ranges, and material properties [13]. Despite this, there are difficulties related to interpreting the information of the reflected waves given the discontinuities and the limited scanning distance covered by the wave with good sensitivity [14]. The high attenuation of guided waves occurs mainly because the propagated wave is

highly dispersive, producing wave packets that spread out in space and time through plate structures. Physically, the dispersions of the ultrasonic pulse as a consequence of the spectral components propagate at different phase velocities [15]. Thus, according to [1], this causes the attenuation of the pulse due to the dispersion or leakage of energy, and increases the complexity of the received signal due to the multiple mode generation [16–18].

Most of the Lamb wave problems are associated with obtaining appropriate dispersion curves and corresponding wave structures [19,20]. There are different analytic and semi-analytic approaches for dispersion curve generation, all of them with different implementation complexities and limitations [20]. This information provided by the dispersion curves includes phase and group velocities, wave number, cut-off frequencies, and the modes with the highest and lowest associated dispersion, among other properties for different propagation modes. Dispersion curves can be obtained experimentally [21–25], numerically [26,27], analytically, and semi-analytical. For instance, the Semi-Analytical Scaled Boundary Finite Element Method (SBFEM) [27,28] is one of the latest approaches defined in the literature. SBFEM is versatile, accurate, and computationally efficient [29]. In the case of the semi-analytic scheme, the waveguide is discretized along the cross-section by using different finite elements and shape functions, while an analytical solution is adopted in the wave propagation direction [30,31].

The spectral elements in the study of guided waves have already been proposed in the literature. Rekatsinas et al. [32–35] investigated the propagation of guided waves in metallic, composite, and sandwich strips with the time-domain spectral finite element method (TDSFE). See [36–38], for instance, which discusses the application of spectral elements as an approach to the study of guided wave propagation.

The application of the SBFEM method to estimate dispersion curves is based on the fact that only the boundary of the computational domain is discretized with finite elements. As indicated in Figure 1, the appropriate one-dimensional functions N are defined by the coordinate η. Few studies on using SBFEM for guided waves' dispersion curve estimations have been reported [36]. The main concerns related to the algorithm's implementation are the associated computational costs and the accuracy for high-order and isoparametric interpolation approaches.
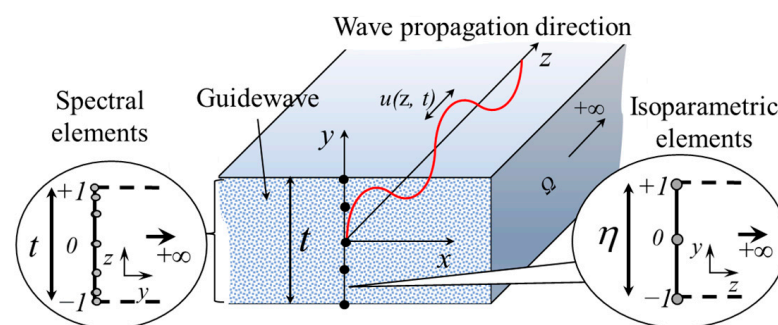

Figure 1. Schematic representation of the plate and SBFEM model.

The contribution of the present work is in investigating the performance of the SBFEM approach in capturing the wave dynamic when isoparametric and high-order spectral elements are used in the discretization of the plate cross-sections. The accuracy in the estimation of the dispersion curves and the wave structure of the wave is evaluated by the comparison between the obtained results using the SBFEM approach (isoparametric and spectral) with the analytical solutions of characteristic equations for symmetric and antisymmetric modes [37]. We also compare the computational time with the number of elements, or the order of interpolation for the spectral elements in functions of the thickness. We present numerical results and infer the performance of the SBFEM method when using spectral elements with Gauss–Lobatto–Legendre nodal distribution. Our results suggest that the method could be useful in terms of performance and effectivity when estimating the dispersion curves for more complex applications associated with different materials,

such as composites and multilayers. Additionally, there is the possibility of considering the effect of viscoelastic properties or embedded materials. However, their performances have not been reported in the literature, and these materials have not been included in the present work.

2. SBFEM for Lamb Waves in Plates

The foundation of the semi-analytic approach is obtaining the wave governing equation by the principle of the virtual work applied to the generation and propagation of the micro-deformation in the material.

Applying the governing equation of linear elastodynamic, the displacements (u), strain (ε), and stress (σ) are expressed by Equation (1),

$$u_{(y,z)} = \begin{bmatrix} u_y \ u_z \end{bmatrix}^T, \ \varepsilon = \begin{bmatrix} \varepsilon_y \ \varepsilon_z \ \gamma_{yz} \end{bmatrix}^T = Lu, \tag{1}$$

where (L) is a three-dimensional differential operator and is used to define the compatibility of Equation (2),

$$\varepsilon = \begin{bmatrix} L_z \frac{\partial}{\partial_z} + L_y \frac{\partial}{\partial_y} \end{bmatrix}^T u; where \ L_z = \begin{bmatrix} 1 & 0 & 0 \\ 0 & 0 & 1 \end{bmatrix}^T, L_y = \begin{bmatrix} 0 & 0 & 1 \\ 0 & 1 & 0 \end{bmatrix}^T. \tag{2}$$

The constitutive equation is expressed as follows,

$$\sigma = \begin{bmatrix} \sigma_y \ \sigma_z \ \tau_{yz} \end{bmatrix}^T = E\varepsilon = ELu, \tag{3}$$

where, E is the elasticity matrix, the real symmetric matrix for isotropic specimen, defined by the following Equation (4), where G is the shear modulus and v is Poisson's ratio:

$$E = \frac{2G}{(1 - 2v)} \begin{bmatrix} 1 - v & v & 0 \\ v & 1 - v & 0 \\ 0 & 0 & \frac{(1-2v)}{2} \end{bmatrix}. \tag{4}$$

In SBFEM, a transformation of global coordinates to local coordinates $(y, z) \rightarrow (\eta, \xi)$ is performed as shown in Figure 1. The principle of virtual work is applied to obtain the governing equation with respect to the coordinate η, where η denotes a parameterization of the boundary of the domain. Lastly, ξ defines the coordinate that points from the origin of the system to the boundary [38]. Based on a variational scheme established by inserting the kinetic and potential energies into Hamilton's equation, a system of linear equations can be constructed with the circular frequency and wavenumber as unknowns under stress-free boundary conditions. Hence, the unknowns can be solved using standard eigenvalue routines. The solution satisfying the eigen equation corresponds to a couple of rotational frequency and wavenumber values (ω, k) obtained using standard eigenvalue routines.

The Scaled Boundary Finite Element Method (SBFEM) is a semi-analytical method that the combines advantages of finite element and boundary element methods simultaneously. The SBFEM equation is solved analytically in the longitudinal direction and exactly converges in the finite-element sense in the thickness direction by using the shape functions. The dimensionless radial coordinate η can be interpreted as a scaling factor. As already mentioned, $\xi = 1$ corresponds to the surface finite element on the boundary. The geometry of the plate is defined by the coordinates of the scaled boundary ξ, η, with $0 \leq \xi \leq 1$, so that the dimensionless coordinate ξ can be interpreted as a scaling factor [39]. The local coordinate η is the one-dimensional representation of a local coordinate system as used in traditional FEM, parallel to the y-axis in this case. Those local coordinates range from 1 and -1 at the edges of the isoparametric and spectral elements (Figure 1). The scaling direction, ξ, is chosen along with the propagation direction, z, obtaining the displacements, within the limit ($z = 0$) as a function of η and ξ, to the z-axis. The cross-sectional domain of

the plate, Ω, may be represented by a system of unidimensional finite elements, due to the simplification attributed to the waveguide symmetry.

3. Implementation

3.1. Discretization Using Isoparametric and High-Order Spectral Elements in the SBFEM

The displacement expressions, discretized over the element domain, can be written in terms of the shape functions $Ni(\eta)$ as shown in Equation (5), in which the displacements of each point along the z-axis is a function of the vertical position of the plate thickness, and the nodal unknown displacements, (U_{yi}, U_{zi}), are expressed in cartesian coordinates,

$$u(z, \eta) = N(\eta)u_n(z). \tag{5}$$

Because the shape functions depend only on η, the derivatives can be separated in terms of the two spatial coordinates for the strain (Equation (6)) and for the stress–displacement relationship (Equation (7),

$$\varepsilon(z, \eta) = B_1 u_{,z}(z) + B_2 u_n(z), \tag{6}$$

$$\sigma = D(B_1 u_{n,z}(z) + B_2 u_n(z), \tag{7}$$

where B_1 and B_2 include the shape functions:

$$B_1 = b_1 N , B_2 = \frac{1}{y_{,n}} b_2 N_{,\eta}, \tag{8}$$

$$N(\eta) = \begin{bmatrix} N_1(\eta) & 0 & N_2(\eta) & 0 & N_3(\eta) & 0 \\ 0 & N_1(\eta) & 0 & N_2(\eta) & 0 & N_3(\eta) \end{bmatrix}, \tag{9}$$

with N_1, N_2 and N_3 expressed in the local coordinates η. Isoparametric elements with three nodes equally spaced are located at local coordinates $\eta0 = -1$, $\eta1 = 0$ and $\eta2 = +1$, so that an element of order p contains $p + 1$ nodes. The curves in Figure 2 illustrate the Lagrange shape functions of a one-dimensional isoparametric element corresponding to the polynomial of order $p = 2$ and the quadratic interpolation functions used as indicated in Equation (10),

$$N_1 = \frac{1}{2}(\eta^2 - \eta), N_2 = (1 - \eta^2), N_3 = \frac{1}{2}(\eta^2 + \eta). \tag{10}$$

Although Lagrange interpolation polynomials may, in principle, be defined for any set of distinct nodes, their properties are critically dependent on node positions. On the other hand, other different nodal distributions can be proposed, so this study employs an example of the Gauss–Lobatto–Legendre nodal distribution, as shown in Figure 2. In this case, the two nodes are located at the extremes $\eta1 = -1$ and $\eta_{p+1} = 1$ [31]. The $p - 1$ nodes, which correspond to internal points according to Gauss–Lobatto–Legendre, GLL, are obtained when they meet the condition of Equation (11),

$$\frac{d}{d\eta} P_p(\eta_i) = 0, i = 2 \dots p, \tag{11}$$

where P_p denotes the Legendre polynomial of order p. The Gauss–Lobatto–Legendre quadrature points are calculated for an element of the given order as follows: For a one-dimensional element of order p with local coordinates η, ranging from -1 to 1, the internal GLL nodes are the roots of the Lobatto polynomial (L) of order $p - 1$, which is defined as the first derivative of the Legendre polynomial (P) of order p, so that:

$$L_{o_{p-1}}(\eta) = \frac{d}{d\eta} P_p(\eta_i) \tag{12}$$

The derivative of the Legendre polynomial P_p of order $p - 1$ yields the Lobatto polynomial, and its roots correspond to the location η of the nodes—Equation (12). These Legendre polynomials for the given order can be obtained as follows, in Equations (13)–(15),

$$P_0(\eta) = 1, \tag{13}$$

$$P_1(\eta) = \eta, \tag{14}$$

$$P_k(\eta) = \frac{2k-1}{k}\eta L_{k-1}(\eta) - \frac{k-1}{k}L_{k-2}(\eta), k = 2, 3, 4\ldots \tag{15}$$

Once the location of the nodes is known, the corresponding shapes functions $N_i(\eta)$ of p order can be constructed using the Lagrange interpolation polynomials [40], obtained from Equation (16),

$$N_i(\eta) = \prod_{\substack{j=1 \\ j \neq i}}^{p+1} \frac{\eta - \eta_j}{\eta_i - \eta_j}, i = 1, 2, \ldots, p + 1. \tag{16}$$

According to the proposed scheme, the first five Legendre polynomials and the corresponding Lobatto polynomials have been obtained as examples. The η roots of the Lobatto polynomial corresponding to the location of the nodes were found by using GLL quadrature points, and these points are included in Table 1. For an element of order p, the $p + 1$ GLL quadrature points are the roots of the polynomial $(1-\eta)2L'p(\eta)$, where $Lp(\eta)$ is the Legendre polynomial of order p. For another order, the same procedure would be repeated.
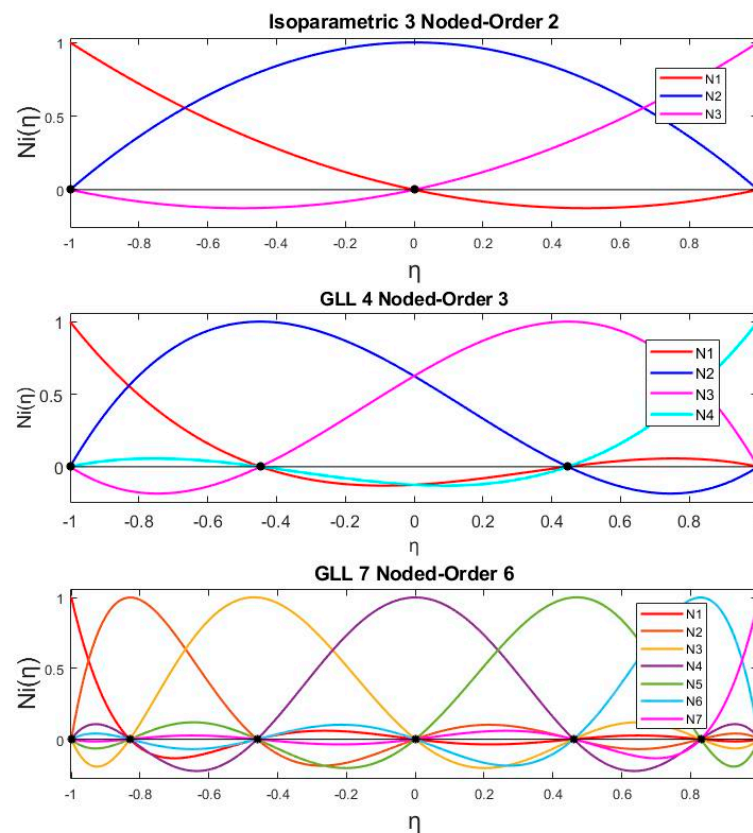
Figure 2. Lagrange shape functions for *GLL* quadrature points.

Table 1. Six Legendre polynomials (*L*), Lobatto polynomials of order $p-1$, and roots (nodes) η.

P	Legendre Polynomial	Lobatto Polynomials	Roots (Nodes) η
1	$L_0(\eta) = 1$	0	± 1
2	$L_1(\eta) = \eta$	$L_0(\eta) = 1$	$\pm 1\ 0$
3	$L_2(\eta) = \frac{1}{2}(3\eta^2 - 1)$	$L_1(\eta) = 3\eta$	$\pm 1 \pm 0.447$
4	$L_3(\eta) = \frac{1}{2}(5\eta^2 - 3)\eta$	$L_2(\eta) = \frac{3}{2}(5\eta^2 - 1)$	$\pm 1 \pm 0.654\ 0$
5	$L_4(\eta) = \frac{1}{8}(35\eta^4 - 30\eta^2 + 3)$	$L_3(\eta) = \frac{5}{2}(7\eta^2 - 3)\eta$	$\pm 1 \pm 0.765$ ± 0.285
6	$L_5(\eta) = \frac{1}{8}(63\eta^4 - 70\eta^2 + 15)\eta$	$L_4(\eta) = \frac{15}{8}(21\eta^4 - 14\eta^2 + 1)$	$\pm 1 \pm 0.830$ $\pm 0.468\ 0$

The shape functions' order of interpolation for spectral elements is evaluated by comparing the computational time and effectiveness (relative error with respect to analytical solution) for equivalent or better results to those obtained with isoparametric elements of order two.

Table 2 shows the shape functions of one spectral element with four nodes (*p* = 3), and Figure 2 shows an example of Lagrange interpolation for order three (*n* = 4) and order six (*n* = 7), based on the GLL approach. The shape functions can be determined for the desired number of nodes, discretizing the entire thickness with a single element.

Table 2. Shape functions for *p* = 3 and 4 nodes (order 3).

η_i	Shape Functions *N*
-1	$N_1(\eta) = \left(\frac{\eta + 0.447}{-1 + 0.447}\right)\left(\frac{\eta - 0.447}{-1 - 0.447}\right)\left(\frac{\eta - 1}{-1 - 1}\right)$
-0.447	$N_2(\eta) = \left(\frac{\eta + 1}{-0.447 + 1}\right)\left(\frac{\eta - 0.447}{-0.447 - 0.447}\right)\left(\frac{\eta - 1}{-0.447 - 1}\right)$
0.447	$N_3(\eta) = \left(\frac{\eta + 1}{0.447 + 1}\right)\left(\frac{\eta + 0.447}{0.447 + 0.447}\right)\left(\frac{\eta - 1}{0.447 - 1}\right)$
$+1$	$N_4(\eta) = \left(\frac{\eta + 1}{1 + 1}\right)\left(\frac{\eta + 0.447}{1 + 0.447}\right)\left(\frac{\eta - 0.447}{1 - 0.447}\right)$

If the order of one element is increased by one, a new additional node should be inserted, and all internal nodes must be repositioned.

To calculate *N*, η with the transformation of coordinates for each element, we use the Jacobian matrix described in Equation (17),

$$|J| = \begin{vmatrix} \partial_\eta y & \partial_\eta z \\ \partial_\xi y & \partial_\xi z \end{vmatrix} = \begin{vmatrix} \partial_\eta y & \partial_\eta z \\ \partial_z y & \partial_z z \end{vmatrix} = \begin{vmatrix} y_{,\eta} & 0 \\ 0 & 1 \end{vmatrix} = y_{,\eta} = \frac{l}{2}. \tag{17}$$

In the case of the plate, the transformation of coordinates for an element is performed via Equation (18),

$$y = \frac{l}{2}(\eta + 1), \tag{18}$$

where *l* is the length of the element.

3.2. Equations of Motion

The guided wave dynamic in the specimen is formulated using an energetic approach by inserting the kinetic and potential energies into the conservative form of Hamilton's principle—Equation (19):

$$\delta U + \delta K = 0. \tag{19}$$

In Equation (20), U is the internal deformation energy and strain energy, and K is the kinetic energy given by Equation (21),

$$\delta U = \int \int_\Omega \delta \varepsilon^T \sigma d\Omega, \tag{20}$$

$$\delta K = \int_0^\infty \delta u_n^T(z) M_0(z) dz, \tag{21}$$

$$M_0 = \int_{-1}^1 N^T \rho N |J| \, d\eta, \tag{22}$$

with ρ as the material density and M_0 the mass matrix in Equation (22). By replacing Equation (6) and solving the integral, the strain energy in Equation (23) is obtained,

$$-\delta u_n^T(z) \int_0^\infty \left(E_0 u_{,zz}(z) + (E_1^T - E_1) u_{n,z}(z) - E_2 u_n(z) \right) dz + \delta u_n^T(0) q_n(0), \tag{23}$$

Here, E_0, E_1 and E_2 in Equations (24)–(26) are the coefficient matrices of the SBFEM scheme, while superscript T denotes the matrix transpose,

$$E_0 = \int_{-1}^1 B_1^T D B_1 |J| \, d_\eta, \tag{24}$$

$$E_1 = \int_{-1}^1 B_2^T D B_1 |J| \, d_\eta, \tag{25}$$

$$E_2 = \int_{-1}^1 B_2^T D B_2 |J| \, d_\eta. \tag{26}$$

Substituting Equations (21) and (23) in Equation (19) yields Equation (27) of the SBFEM, with semi-analytical equations for the displacements in the cross-section, since the nodal displacements $u_n(z)$ can be arbitrary analytic functions of z, while the y-direction is discretized along the element direction,

$$-\delta u_n^T(z) \int_0^\infty \left(E_0 u_{,zz}(z) + (E_1^T - E_1) u_{n,z}(z) - E_2 u_n(z) - M_0(z) \right) dz = 0. \tag{27}$$

The solutions of the displacement functions in Equation (27) yield:

$$u_n(z) = e^{\lambda z - i\omega \, t} \hat{u}, \tag{28}$$

where ω is the angular frequency, t is the time, i is the imaginary unit, and $\hat{u}$ is the complex displacement vector. The modes that can propagate are defined by Equation (29),

$$\lambda = iK, \tag{29}$$

where K is the wave number in the z-direction for a particular wave mode. Substituting Equation (29) into Equation (27) yields Equation (30). The generalized SBFEM governing equation for a stress-free plate is obtained as

$$\left(\lambda^2 E_0 + \lambda (E_1^T - E_1) - E_2 + \omega^2 M_0 \right) \hat{u}_n = 0 \tag{30}$$

For a given specific frequency ω, Equation (30) establishes a second-order polynomial eigenvalue problem for the eigenvalues λ and the eigenvectors $\hat{u}_n$, which can be solved numerically by standard procedures.

The wave structures of each mode are the eigenvectors $\hat{u}_n$, and are the vectors of the global displacement amplitudes of all nodes of the discretization. The wave structure is useful when investigating sensitivity for certain defects and scanning distances.

3.3. Algorithm for Computing Dispersion Curves by SBFEM

Figure 3 shows a schematic representation of the proposed algorithm for estimating the dispersion curves by SBFEM. The first step is to set the model parameters by defining the plate thickness t, the material, and the density ρ, as well as the elasticity matrix E, which includes the shear modulus G and Poisson's ratio ν.
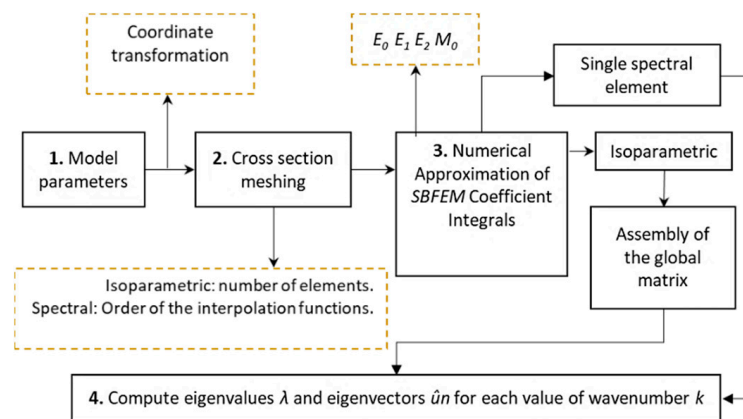

Figure 3. Schematic diagram of the proposed algorithm for plotting dispersion curves by SBFEM.

The second step is the meshing of the plate cross-section. So, the number of isoparametric elements and the order of the shape functions in the case of spectral elements are determined.

The third step is the calculation of the coefficient matrices E_0, E_1, E_2, and M_0 using integration and the Gaussian quadrature method of approximation for the isoparametric and spectral methods, respectively. The coefficient or elementary matrices are assembled into a global matrix with size as a function of the number of elements used.

The fourth step is to solve the eigenvalue problem to find the eigenvalues ω and their corresponding eigenvectors λ for each value of the wavenumber k. as a solution, we obtain the (ω,k) couples that are the basis for generating the dispersion curves, according to the following equations:

$$C_p = \frac{\omega}{k}, \text{where } \omega = 2\pi f, \tag{31}$$

$$C_g = \frac{d\omega}{dk} \tag{32}$$

The numerical results of the two discretization schemes are compared with the analytical solution to verify the accuracy of the method. The maximum frequency of the dispersion curves is approximated to obtain a wavelength λ equal to or greater than the structural thickness.

3.4. Analytical Solution of Lamb Waves

The analytical estimation of the dispersion curves is performed by the Rayleigh–Lamb equations for plates considering only real values for wavenumbers k. This is determined by

the following implicit equations: for symmetrical *S* Lamb waves, Equation (33), and for antisymmetric *A* Lamb waves, Equation (34),

$$\frac{\tan(qh)}{q} + \frac{4k^2 p\ \tan(ph)}{(q^2 - k^2)^2} = 0 \ for \ (S), \tag{33}$$

$$q\ \tan(qh) + \frac{(q^2 - k^2)^2\ \tan(ph)}{4k^2 p} = 0 \ for \ (A), \tag{34}$$

where the *p* and *q* parameters are presented by the following set of equations:

$$p = \sqrt{\frac{\omega^2}{C_L^2} - K^2}, \tag{35}$$

$$q = \sqrt{\frac{\omega^2}{C_T^2} - K^2} \tag{36}$$

The solutions to Equations (33) and (34) are obtained via an implicit k and ω equation problem. Thus, the real roots are computed with a MATLAB program set up using the *findAllZeros* function with a tolerance of 1×10^{-16}. The in-plane and out-of-plane particle motions across the plate thickness are described by the wave structures, and are obtained for symmetric and antisymmetric modes from the following equations.
Symmetric solution:

$$u_x = -2k^2 q \cos(qd) \cos(py) + q(k^2 - q^2) \cos(pd)\ \sin(qy), \tag{37}$$

$$u_y = -2ikpq \cos(qd) \sin(py) - ik(k^2 - q^2) \cos(pd)\ \sin(qy) \tag{38}$$

Antisymmetric solution:

$$u_x = -2k^2 q\ \sin(qd) \sin(py) + q(k^2 - q^2)\ \sin(pd)\ \sin(qy), \tag{39}$$

$$u_y = -2ikpq \sin(qd) \cos(py) + ik(k^2 - q^2) \sin(pd)\ \cos(qy). \tag{40}$$

Figure 4 shows the direction of in-plane and out-of-plane displacement for modes A and S with respect to the plane of symmetry at the center of the plate. The amplitude along the thickness is fully described by the wave structures.
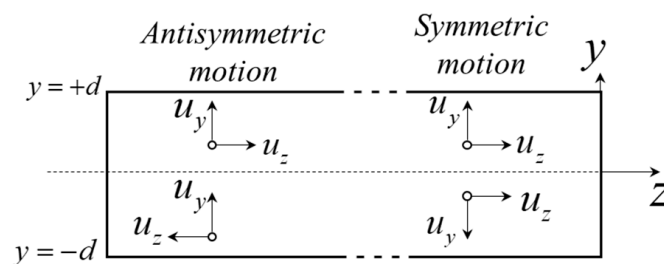

Figure 4. Symmetric and antisymmetric particle motion across the plate thickness.

4. Results and Discussion

In this section, the dispersion curves for several plates are calculated by the approaches of the SBFEM and the analytic equations. In the first case, the two meshing schemes, isoparametric and spectral elements are considered, and in the second case the Rayleigh–Lamb equations are considered. In both cases, the dispersion curves are generated for an ASTM A106-B steel plate *E* = 212 GPa, Poisson's ratio 0.289, mass density 7750 kg/m^3, and shear velocity 3185 m/s.

4.1. Numerical Results for Isoparametric Elements

The SBFEM performance in terms of computing time and accuracy is strongly related to the discretization of the cross-section. In the absence of a criterion for optimum discretization, calculations are performed using six to twelve nodes per wavelength (δ) for isoparametric elements and different interpolation orders for spectral elements. The results are used to estimate the number of nodes required to ensure the efficiency and convergence of the SBFEM. The accuracy for the mode of interest with the highest frequencies (λmin) according to Equation (41) will be considered,

$$l_{\min} = \frac{C_T}{(nodes\ per\ unit\ of\ \lambda)\ f_{\max}} = \frac{\lambda_{\min}}{\delta}. \tag{41}$$

Numerical results with different numbers of nodes were obtained and compared with the analytical solution. In Figure 5, the phase velocity versus frequency for the S and A modes are plotted. In Figure 5, red is used for the isoparametric elements, black for the analytical ones, and green for the spectral elements. A good agreement is observed for the given frequency range for both the curves calculated with isoparametric and spectral elements as shown in Table 3.
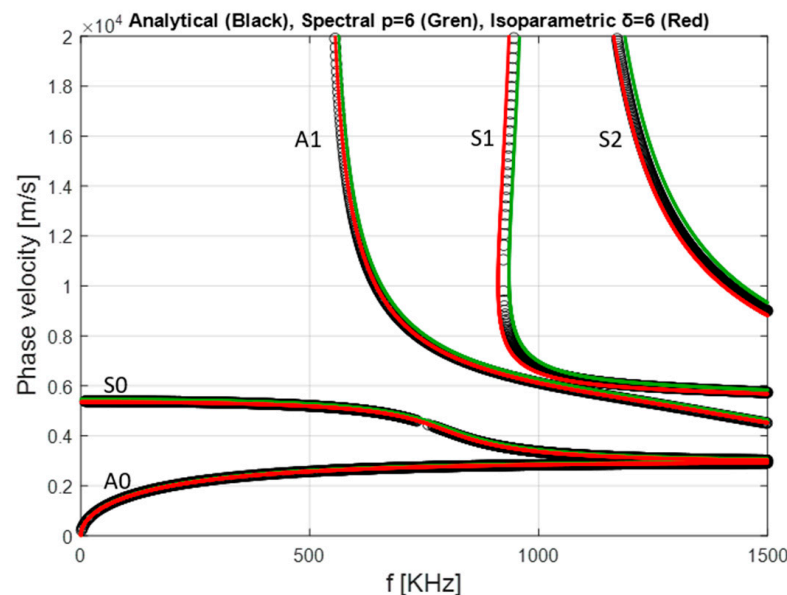

Figure 5. Phase velocity dispersion curves were calculated by SBFEM with isoparametric and spectral elements for a 3 mm-thick isotropic plate. Symmetric Sn and antisymmetric An (n = 0, 1, 2, …) modes.

Small deviations are observed for the *S* and *A* modes at high frequencies, *f* > 900 kHz. This is to be expected, since the higher the frequency of the mode, the shorter its wavelength, requiring a greater number of nodes to capture the dynamics of the system.

Figure 6 shows the group velocity dispersion curves of the modes that can propagate in the steel plate. Using the SBFEM with six nodes per wavelength (δ) for isoparametric and only one element of order six for spectral elements has been done for the discretization of the cross-section. The results obtained from both approaches are in excellent agreement with the analytical solution.

Table 3. Percentage of variation of Cp (m/s) for modes S0, S1, A0 and A1 for specific frequencies as a function of the number of elements n. Frequency *f* in kHz.

| Number of Elements (*n*)	S0 at *f* = 400	S0 at *f* = 800	S1 at *f* = 1000	S1 at *f* = 1200	S2 at *f* = 1200	S2 at *f* = 1400	A0 at *f* = 400	A0 at *f* = 800	A1 at *f* = 1000	A1 at *f* = 1400
6	5258.14	4193.82	6527.95	5933.52	16,736.26	10,080.50	2447.16	2771.13	6118.18	4843.82
Percentage of variation	0.46	0.26	3.25	1.65	1.69	1.88	0.16	0.05	0.08	0.41
28	5258.13	4192.55	6524.64	5931.94	16,672.32	10,053.50	2446.88	2770.32	61,160.62	4836.97
Percentage of variation	0.46	0.23	3.30	1.67	2.06	2.14	0.17	0.05	0.11	0.26
Order (*p*)										
4	5358.32	4316.36	7020.75	6178.83	16,076.90	10,204.81	2476.76	2807.94	6271.53	4979.68
Percentage of variation	1.44	3.19	4.06	2.42	5.56	0.67	1.05	1.28	2.43	3.22
6	5358.31	4312.78	6981.31	6143.07	18,798.51	10,724.92	2476.47	2805.44	6261.02	4952.14
Percentage of variation	1.43	3.11	3.47	1.83	4.30	4.39	1.04	1.19	2.26	2.65
8	5358.36	4312.78	6981.25	6142.48	18842	10,740.53	2476.47	2805.44	6260.99	4952.05
Percentage of variation	1.44	3.11	3.47	1.82	4.54	4.54	1.04	1.19	2.26	2.65
12	5358.36	4312.78	6981.25	6142.48	18,842	10,740.50	2476.47	2805.44	6260.99	4952.05
Percentage of variation	1.44	3.11	3.47	1.82	4.54	4.54	1.04	1.19	2.26	2.65
Analytical	5282.51	4182.90	6747.02	6032.88	18,023.09	10,273.77	2450.99	2772.41	6122.81	4824.21
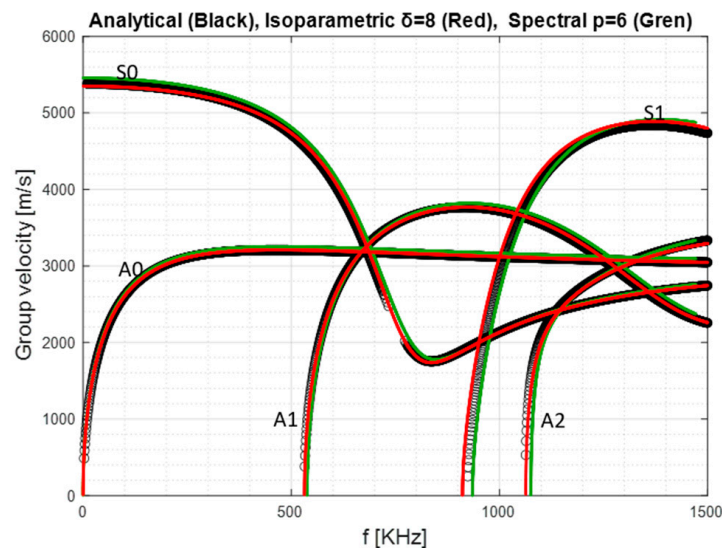
Figure 6. Group velocity dispersion curves calculated by SBFEM with isoparametric and spectral elements for a 3 mm-thick isotropic plate. Symmetric *Sn* and antisymmetric *An* (*n* = 0, 1, 2, …) modes.

4.2. Spectral Elements

In this case, the dispersion curves have been generated with a six-order spectral element with the nodes located at the GLL points in the material. The results have been compared with the isoparametric elements and with the analytical solution. The phase velocity and group velocity dispersion curves generated with a spectral element are presented in Figures 5 and 6 for modes S and A. The curves generated with spectral elements are in good agreement with those generated with isoparametric elements and analytically. The performance, computing time and accuracy of the spectral approach for a six-order element is preserved even when a 50 mm-thick plate is considered, as shown in Figure 7a,b. As a result, it can be concluded that the spectral elements showed a fast convergence, leading to excellent results with good accuracy. To illustrate numerical results for the spectral element approach, one six-order spectral element is required for obtaining convergence in the S1 mode estimation. Selecting the appropriate element order is fundamental, since the benefit of increasing the element order is imperceptible when convergence is achieved. These results reveal a comparable performance in the dispersion curves' estimation when fewer nodes per wavelength in the spectral scheme are implemented, compared with the isoparametric elements approach.
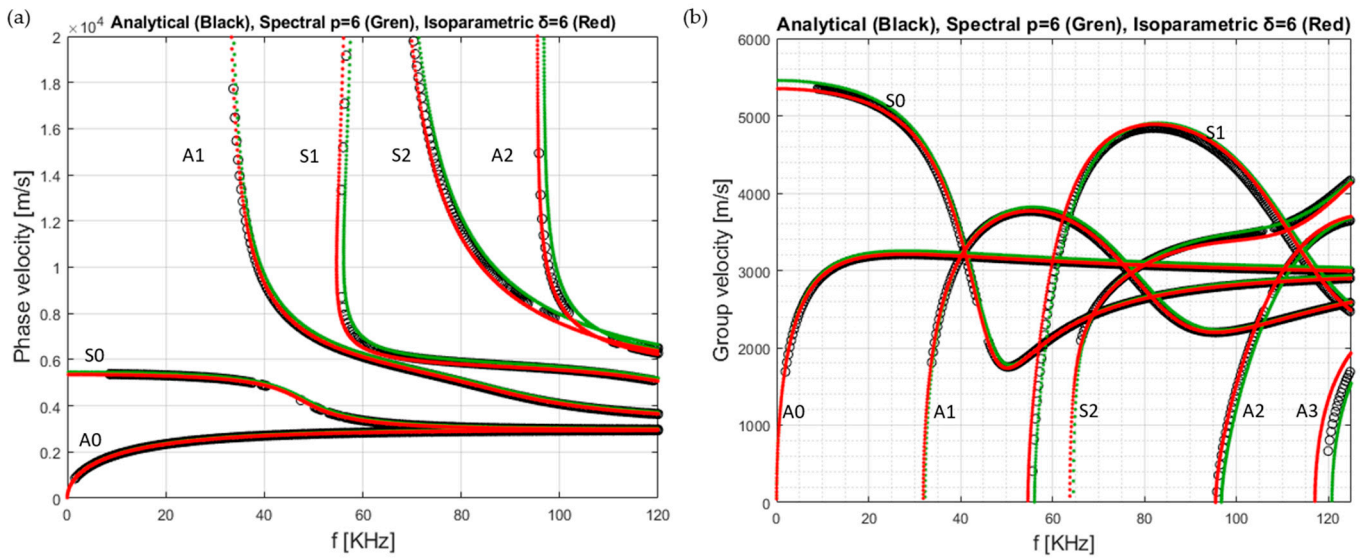
Figure 7. Dispersion curves given by the SBFEM method with isoparametric and spectral elements for a 50 mm-thick isotropic plate. (**a**) Phase velocity. (**b**) Group velocity. Symmetric *Sn* and antisymmetric *An* (*n* = 0, 1, 2, . . .) modes.

4.3. Quantitative Evaluation of SBFEM Method

Once the dispersion curves are generated, a quantitative study of convergence is performed for the SBFEM method with isoparametric and spectral elements. The discretization is set up as described in Figure 1. The phase velocities are presented in Figure 8 for wave mode S1 and a plate thicknesses t between 1 mm and 100 mm. Figure 8 shows the phase velocity estimation for different nodes per wavelength, where the curves converge for six nodes per wavelength (δ) for all studied plate thicknesses. The same convergence is evident for high-frequency modes, such as the S3 mode in a 1 mm-thick plate.
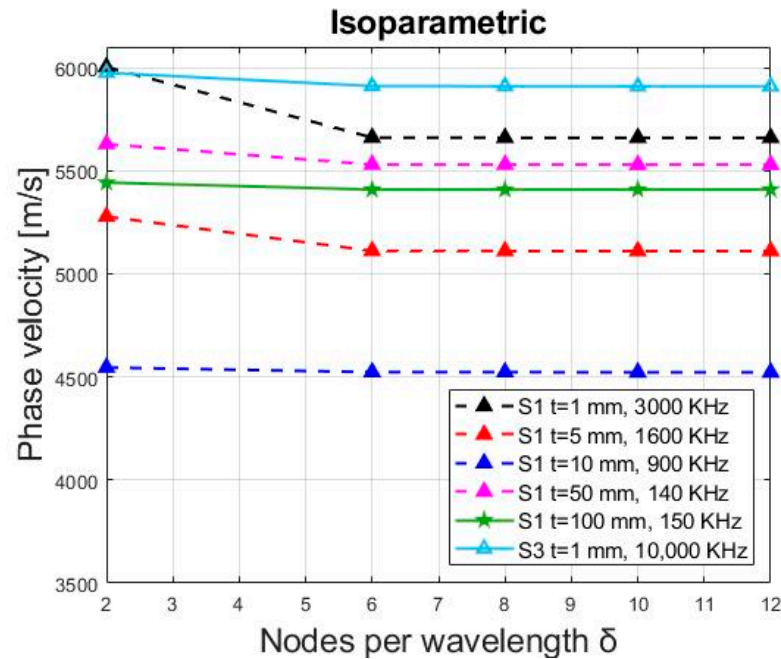

Figure 8. Number of nodes per wavelength required for convergence with plate thicknesses up to 100 mm.

On the other hand, in Figure 9, the plate thickness is independent of the order of interpolation for spectral elements greater than six for the phase velocity estimations. The

same behavior is observed for the rest of the dispersion curves. In the same figure, a higher slope for orders less than p = 4 is seen. Based on the previous results, the spectral discretization is independent of the plate thickness in terms of computational time and accuracy. For lower-order modes, convergence is achieved with fewer nodes. The computational efficiency is improved by implementing the spectral elements, which is much more noticeable with increasing plate thickness. Once the method presents convergence, the value obtained does not present modifications due to the increase in the interpolation order.
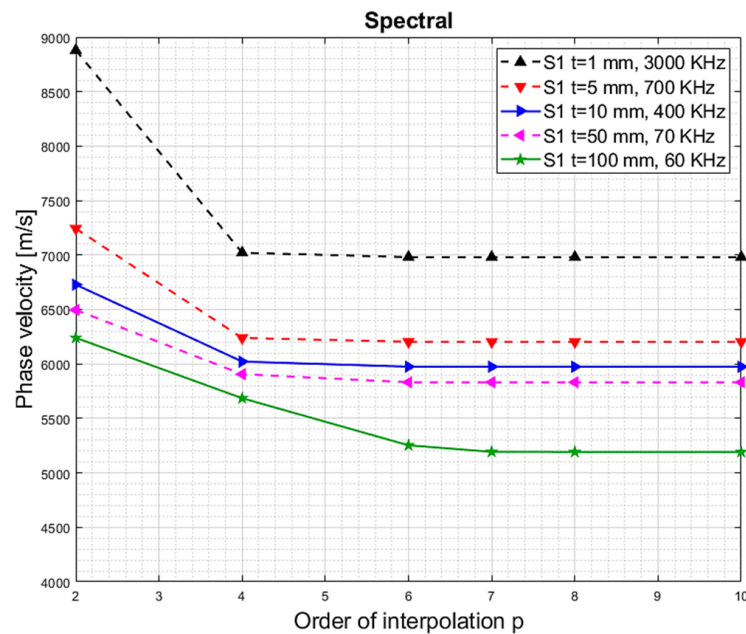

Figure 9. Comparison of the convergence curves for spectral elements of different orders of interpolation p and thicknesses between 1 mm and 100 mm.

The combined results of Figures 9 and 10 provide an appropriate basis for formulating a guideline to generate an efficient discretization. In all cases in this work, a selection of more than six nodes per wavelength, or an interpolation order greater than eight, are adequate to generate the dispersion curves. However, in the present work, a relationship to determine the interpolation order as a function of frequency for higher-order modes is not included because, in practical terms, integrity evaluation by guided waves is always preferred to launch the lowest-mode waves, due to the possibility of multimode activation at high frequencies.

Figure 10 summarizes the behavior of the semi-analytical and analytical methods studied in this work, where the computational time is related to the thickness of the plate in the case of the semi-analytical approach. The two approaches were tested on a PC (Intel Ci7-6820HQ CPU at 2.7 GHz, 8 GB RAM) with one stepwise increment of k for the SBFEM approaches. As expected, as the thickness increases in the SBFEM isoparametric scheme, the number of elements increases, increasing the running time for the calculation of the dispersion curve. The minimum number of isoparametric elements required for the calculation of the dispersion curves in this study is six nodes per wavelength, which corresponds to an optimized value of the number of elements. The numerical results show a quadratic relationship between the number of elements and the running time, as shown in Figure 10.

On the other hand, the spectral elements have a good convergence, which is independent of the plate thickness. The computational time is the same across the range of thicknesses studied.

Since our objective is to investigate the performance of the SBFEM method in capturing the wave dynamics, the spectral elements within the Gaussian–Lobatto–Legendre

quadrature yield achievable computational times for the practical range of plate thicknesses, making this a recommendable option.
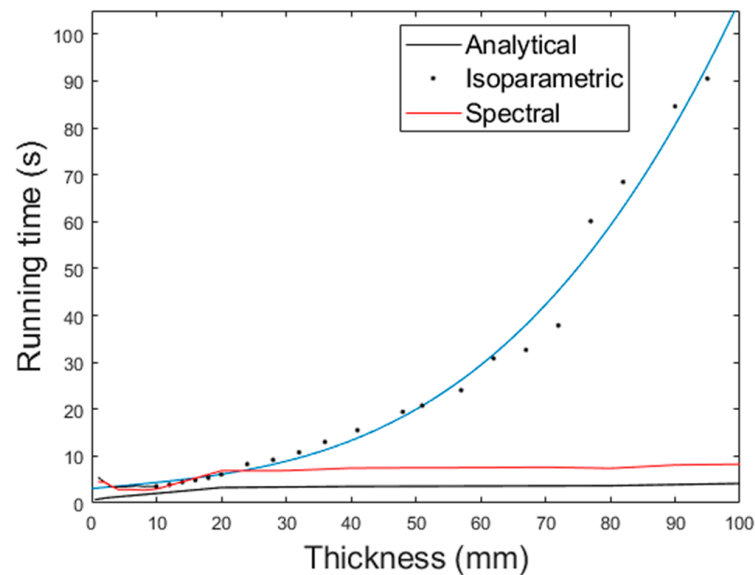

Figure 10. Interpolation order required for convergence with plate thicknesses up to 100 mm.

4.4. Wave Structure across the Plate Thickness

As noted above, the wave modes' characteristics can be very different for the same waveguide and frequency range. For this reason, wave structures for the S and A modes are generated with the SBFEM method from the studied models, and are compared with the analytical solution for validation. This information is helpful for the selection of possible points of dispersion curves, leading to a valid test. The wave structures are generated, with semi-analytical methods using isoparametric and spectral elements, from the eigenvectors of Equation (30). These wave structures are compared with those generated analytically using Equations (37) to (40). Figure 11 shows the good agreement of the results, calculated with low computational cost. Figure 11 shows the in-plane (uz) and out-of-plane (uy) displacement for S0 mode at frequency f = 400 kHz. The results in Figure 11a were generated analytically, those in Figure 11b semi-analytically using isoparametric elements, and those in Figure 11c using spectral elements.
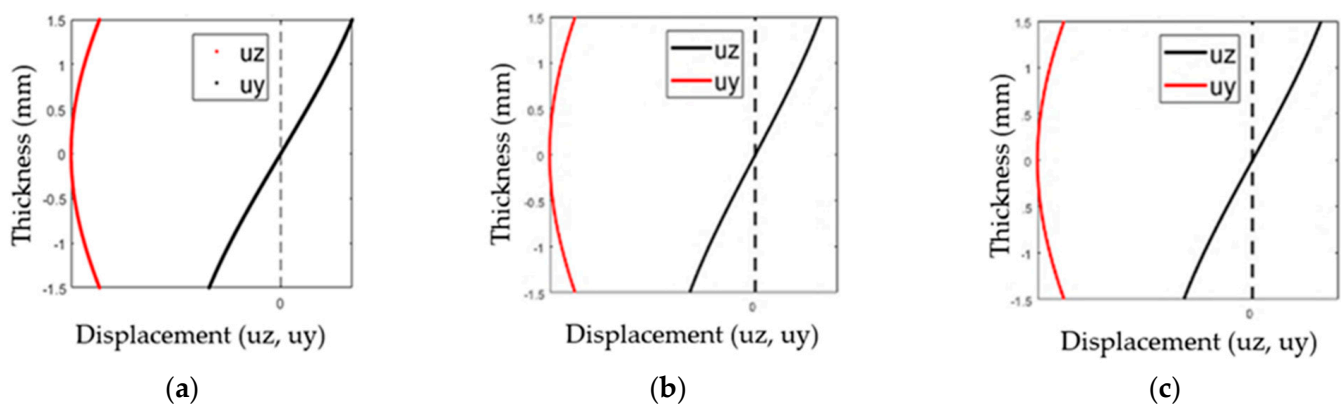

(a)	(b)	(c)

Figure 11. The wave structure of S0 mode at 500 kHz. (**a**) Analytical solution. (**b**) SBFEM isoparametric elements. (**c**) SBFEM spectral elements.

5. Conclusions

The results of the benchmark tests show that spectral finite element methods are an efficient numerical tool, requiring fewer nodes to calculate reliable dispersion curves of ultrasonic guided waves on plates. The benchmark test results demonstrate that the spectral finite element method applied to dispersion curve calculation in plates requires fewer nodes than the isoparametric method, achieving convergence with a total of eight nodes. Greater plate thickness requires a larger number of isoparametric elements, thus demanding a longer computational time. A quadratic relationship between the increase in the running time and the increase in the thickness was found for the dispersion curves' estimation in the isoparametric elements approach.

The Scaled Boundary Finite Element Method implemented with spectral elements required lower computational times than the quadratic isoparametric elements. Despite this, the generated dispersion curves show good agreement for the frequency range of interest. Consequently, the spectral elements yield reliable data, and could be implemented in more complex conditions, as they do not require the construction of a global matrix.

Isoparametric elements and spectral elements show good convergence of properties with a similar quality of results. In general, the spectral elements under the Gaussian–Lobatto–Legendre quadrature schemes achieve better performance by efficiently solving the coefficient integrals and not requiring the assembly of a global matrix. These results are in agreement with those published by Gravenkamp et al. [30] and Willberg et al. [31]. An advantage of the Gaussian–Lobatto–Legendre scheme is that it concentrates the nodes near the surface, where the wave profiles register high displacements, giving a possible physical meaning to the better performance of the approach.

In general, it can be concluded that spectral elements require a lower number of nodes per wavelength, which is independent of the plate thickness. In isoparametric approaches, however, the number of nodes required increases with increasing thickness in order to achieve a similar performance in calculating the dispersion of ultrasonic guided waves for the nondestructive inspection of plates.

Author Contributions: C.A.G.-P. Wrote the manuscript; C.A.G.-P. and J.E.-Q. Contributed to the interpretation of the results; C.A.A.-M., O.A.G.-E. and J.E.-Q. formal analysis; D.Y.P.-B. supervision; C.A.G.-P., O.A.G.-E. and J.E.-Q. carried out the numerical simulations and analyzed the data. All authors have read and agreed to the published version of the manuscript.

Institutional Review Board Statement: Not applicable.

Informed Consent Statement: Not applicable.

Data Availability Statement: The data presented in this study are available in the article.

References

1.　Rose, J.L. *Ultrasonic Waves in Solid Media*; Cambridge University Press: Cambridge, MA, USA, 2014. [CrossRef]
2.　Zhu, W.; Xu, Z.; Xiang, Y.; Liu, C.; Deng, M.; Qiu, X.; Sun, D.; Xuan, F. Nonlinear ultrasonic detection of partially closed cracks in metal plates using static component of lamb waves. *NDT E Int.* **2021**, *124*, 102538. [CrossRef]
3.　Haider, M.F.; Joseph, R.; Giurgiutiu, V.; Poddar, B. An efficient analytical global–local (AGL) analysis of the Lamb wave scattering problem for detecting a horizontal crack in a stiffened plate. *Acta Mech.* **2020**, *231*, 577–596. [CrossRef]
4.　Zima, B.; Kędra, R. Detection and size estimation of crack in plate based on guided wave propagation. *Mech. Syst. Signal Process.* **2020**, *142*, 106788. [CrossRef]
5.　Nagy, P.B.; Simonetti, F.; Instanes, G. Corrosion and erosion monitoring in plates and pipes using constant group velocity Lamb wave inspection. *Ultrasonics* **2014**, *54*, 1832–1841. [CrossRef]
6.　Ding, X.; Xu, C.; Deng, M.; Zhao, Y.; Bi, X.; Hu, N. Experimental investigation of the surface corrosion damage in plates based on nonlinear Lamb wave methods. *NDT E Int.* **2021**, *121*, 102466. [CrossRef]

7. Goyal, D.; Vanraj; Pabla, B.; Dhami, S. Non-contact sensor placement strategy for condition monitoring of rotating machine-elements. *Eng. Sci. Technol. Int. J.* **2019**, *22*, 489–501. [CrossRef]

8. Poddar, B.; Giurgiutiu, V. Scattering of Lamb waves from a discontinuity: An improved analytical approach. *Wave Motion* **2016**, *65*, 79–91. [CrossRef]

9. Ochôa, P.; Villegas, I.F.; Groves, R.M.; Benedictus, R. Diagnostic of manufacturing defects in ultrasonically welded thermoplastic composite joints using ultrasonic guided waves. *NDT E Int.* **2019**, *107*, 102126. [CrossRef]

10. Peñaloza-Peña, S.A.; Galvis, G.C.; Quiroga, M.J. Failure detection in a pressure vessel using acoustic emissions technology. *Rev. UIS Ing.* **2019**, *18*, 147–156. [CrossRef]

11. Quiroga, J.E.; Villamizar, R.; Mujica, L.E.; Quiroga, J.; Ruiz, M. Guided ultrasonic wave for monitoring stress levels. In Proceedings of the 7th ECCOMAS Thematic Conference on Smart Structures and Materials (SMART 2015), Azores, Portugal, 3–6 June 2015.

12. Mei, H.; Haider, M.F.; James, R.; Giurgiutiu, V. Pure S0 and SH0 detections of various damage types in aerospace composites. *Compos. Part B Eng.* **2020**, *189*, 107906. [CrossRef]

13. Lamb, H. On waves in an elastic plate. *Proc. R. Soc. London. Ser. A Contain. Pap. Math. Phys. Character* **1917**, *93*, 114–128. [CrossRef]

14. Schaal, C.; Mal, A. Lamb wave propagation in a plate with step discontinuities. *Wave Motion* **2016**, *66*, 177–189. [CrossRef]

15. Wilcox, P.; Lowe, M.; Cawley, P. Wilcox-2001-The effect of dispersion on long-range inspection using ultrasonic guided waves. *Ndt E Int.* **2001**, *34*, 1–9. [CrossRef]

16. Draudviliene, L.; Tumsys, O.; Mazeika, L.; Zukauskas, E. Estimation of the Lamb wave phase velocity dispersion curves using only two adjacent signals. *Compos. Struct.* **2021**, *258*, 113174. [CrossRef]

17. Groth, E.B.; Iturrioz, I.; Clarke, T.G.R. The dispersion curve applied in guided wave propagation in prismatic rods. *Lat. Am. J. Solids Struct.* **2018**, *15*, 1–27. [CrossRef]

18. Workman, G.L.; Moore, P.O. *Nondestructive Testing Handbook, Ultrasonic Testing*, 3rd ed.; American Society for Nondestructive Testing: Columbus, OH, USA, 2007; Volume 7.

19. Nissabouri, S.; El Allami, M.; Boutyour, E.H. Quantitative evaluation of semi-analytical finite element method for modeling Lamb waves in orthotropic plates. *Comptes Rendus. Mec.* **2020**, *348*, 335–350. [CrossRef]

20. Bartoli, I.; Marzani, A.; di Scalea, F.L.; Viola, E. Modeling wave propagation in damped waveguides of arbitrary cross-section. *J. Sound Vib.* **2006**, *295*, 685–707. [CrossRef]

21. Gao, X.; Tian, Y.; Jiao, J.; Gao, J.; Li, C. An accurate measurement method of lamb wave phase velocity based on clustering algorithms. *Measurement* **2022**, *195*, 111178. [CrossRef]

22. El Bakkali, M.; Lhémery, A.; Baronian, V.; Chapuis, B. Guided wave propagation and scattering in pipeworks comprising elbows: Theoretical and experimental results. *J. Phys. Conf. Ser.* **2015**, *581*, 012011. [CrossRef]

23. Crespo, B.H.; Courtney, C.R.P.; Engineer, B. Calculation of Guided Wave Dispersion Characteristics Using a Three-Transducer Measurement System. *Appl. Sci.* **2018**, *8*, 1253. [CrossRef]

24. Serey, V.; Quaegebeur, N.; Micheau, P.; Masson, P.; Castaings, M.; Renier, M. Selective generation of ultrasonic guided waves in a bi-dimensional waveguide. *Struct. Heal. Monit.* **2019**, *18*, 1324–1336. [CrossRef]

25. Galvis, L.; Quiroga, J.; González-Estrada, O.A. Numerical modelling of guided waves dispersion curves in an aluminium flat plate by finite element analysis. *J. Phys. Conf. Ser.* **2019**, *1386*, 012117. [CrossRef]

26. Chen, Q.; Xu, K.; Ta, D. High-resolution Lamb waves dispersion curves estimation and elastic property inversion. *Ultrasonics* **2021**, *115*, 106427. [CrossRef] [PubMed]

27. Ding, X.; Zhao, Y.; Hu, N.; Liu, Y.; Zhang, J.; Deng, M. Experimental and numerical study of nonlinear lamb waves of a low-frequency S0 mode in plates with quadratic nonlinearity. *Materials* **2018**, *11*, 2096. [CrossRef]

28. Gunawan, A.; Hirose, S. Boundary element analysis of guided waves in a bar with an arbitrary cross-section. *Eng. Anal. Bound. Elem.* **2005**, *29*, 913–924. [CrossRef]

29. Gravenkamp, H. Efficient simulation of elastic guided waves interacting with notches, adhesive joints, delaminations and inclined edges in plate structures. *Ultrasonics* **2018**, *82*, 101–113. [CrossRef]

30. Gravenkamp, H.; Song, C.; Prager, J. A numerical approach for the computation of dispersion relations for plate structures using the Scaled Boundary Finite Element Method. *J. Sound Vib.* **2012**, *331*, 2543–2557. [CrossRef]

31. Willberg, C.; Duczek, S.; Perez, J.V.; Schmicker, D.; Gabbert, U. Comparison of different higher order finite element schemes for the simulation of Lamb waves. *Comput. Methods Appl. Mech. Eng.* **2012**, *241–244*, 246–261. [CrossRef]

32. Rekatsinas, C.S.; Nastos, C.V.; Theodosiou, T.C.; Saravanos, D.A. A time-domain high-order spectral finite element for the simulation of symmetric and anti-symmetric guided waves in laminated composite strips. *Wave Motion* **2015**, *53*, 1–19. [CrossRef]

33. Kudela, P.; Krawczuk, M.; Ostachowicz, W. Wave propagation modelling in 1D structures using spectral finite elements. *J. Sound Vib.* **2007**, *300*, 88–100. [CrossRef]

34. Minoli, C.A.A.; Kopriva, D.A. Discontinuous Galerkin spectral element approximations on moving meshes. *J. Comput. Phys.* **2011**, *230*, 1876–1902. [CrossRef]

35. Barouni, A.K.; Saravanos, D.A. A layerwise semi-analytical method for modeling guided wave propagation in laminated composite infinite plates with induced surface excitation. *Wave Motion* **2017**, *68*, 56–77. [CrossRef]

36. Gravenkamp, H.; Saputra, A.A.; Duczek, S. High-Order Shape Functions in the Scaled Boundary Finite Element Method Revisited. *Arch. Comput. Methods Eng.* **2021**, *28*, 473–494. [CrossRef]

37. Predoi, M.V. Guided waves dispersion equations for orthotropic multilayered pipes solved using standard finite elements code. *Ultrasonics* **2014**, *54*, 1825–1831. [CrossRef]
38. Deeks, A.J.; Wolf, J.P. A virtual work derivation of the scaled boundary finite-element method for elastostatics. *Comput. Mech.* **2002**, *28*, 489–504. [CrossRef]
39. Song, C.; Wolf, J.P. The scaled boundary finite-element method–a primer: Solution procedures. *Comput. Struct.* **2000**, *78*, 211–225. [CrossRef]
40. Vu, T.H.; Deeks, A.J. Use of higher-order shape functions in the scaled boundary finite element method. *Int. J. Numer. Methods Eng.* **2005**, *65*, 1714–1733. [CrossRef]